



Convergence and efficiency of global bases using proper orthogonal decomposition for capturing wind turbine wake aerodynamics

Juan Felipe Céspedes Moreno¹, Juan Pablo Murcia León¹, and Søren Juhl Andersen²

¹Department of Wind and Energy Systems, Technical University of Denmark, Frederiksborgvej 399, Roskilde, 4000, Denmark

²Department of Wind and Energy Systems, Technical University of Denmark, Anker Engellunds Vej 1, Kgs. Lyngby, 2800, Denmark

Correspondence: Juan Felipe Céspedes Moreno (jfc@dtu.dk)

Received: 2 July 2024 – Discussion started: 16 July 2024

Revised: 20 December 2024 – Accepted: 6 January 2025 – Published: 21 March 2025

Abstract. Wind turbine wakes affect power production and loads but are highly turbulent and therefore complex to model. Proper orthogonal decomposition (POD) has often been applied for reduced-order models (ROMs), as POD yields an orthogonal basis optimal in terms of capturing the turbulent kinetic energy content. POD is typically used to understand flow physics and reconstruct a specific flow case. However, reduced-order models have been proposed for predicting wind turbine wake aerodynamics by applying POD on multiple flow cases with different governing parameters to derive a global basis intended to represent all flows within the parameter space. This article evaluates the convergence and efficiency of global POD bases covering multiple cases of wind turbine wake aerodynamics in large wind farms. The analysis shows that the global POD bases have better performance across the parameter space than the optimal POD basis computed from a single dataset. The error associated with using a global basis across the parameter space of reconstructions decreases and converges as the dataset is expanded with more flow cases, and there is a low sensitivity as to which datasets to include. It is also shown how this error is an order of magnitude smaller than the truncation error for 100 modes. Finally, the global basis has the advantage of providing consistent physical interpretability of the highly turbulent flow within wind farms.

1 Introduction

The proper orthogonal decomposition (POD) is a classic data-driven method for decomposing fluctuations of turbulent flows into orthogonal modes, which provide an optimal linear decomposition in terms of the variance (Lumley, 1967; Berkooz et al., 1993). POD has been applied to a vast range of flow scenarios, and the POD modes are typically used for one of two main applications. One, the modes can provide a physical interpretation of dominant coherent structures in complex turbulent flow (e.g., Sirovich, 1987; George, 1988; Neumann and Wengle, 2004; Meyer et al., 2007). Two, a truncated set of the modes can be used to construct reduced-

order models (ROMs) (e.g., Smith et al., 2005; Noack et al., 2011; Semaan et al., 2016; Taira et al., 2017).

However, an optimal reconstruction in terms of variance might not always be the most desirable basis for creating ROMs. Alternative bases can for instance be derived by changing the norm to optimize other quantities instead of variance, e.g., enthalpy, enstrophy, and dissipation (Colonius et al., 2002; Lee and Dowell, 2020; Olesen et al., 2023). Emphasis can also be on the spectral content by performing POD in the frequency domain using spectral POD (Sieber et al., 2016) or the related dynamic mode decomposition (Schmid, 2010), which does not provide orthogonal bases. Furthermore, nonlinear bases can be formed using autoencoders, which constitute a nonlinear generalization of POD through

an artificial neural network (ANN) (Hinton and Salakhutdinov, 2006; Vinuesa and Brunton, 2022). Autoencoders are specifically designed to reduce the number of degrees of freedom required to describe a dataset but might lack physical interpretability.

Irrespective of the decomposition method, the resulting bases are typically applied to data from a single flow case, which corresponds to a single point in parameter space. A single flow case would in the present content correspond to the inflow to a particular wind turbine in a wind farm operating at a single C_T value (Andersen et al., 2014; Debnath et al., 2017; Bastine et al., 2018; Hamilton et al., 2018). However, efforts have been made to transition between different bases to cover different flow cases in parametric studies (Christensen et al., 1999; Stankiewicz et al., 2017; Xiao et al., 2017). Conversely, recent developments (Andersen and Murcia Leon, 2022; Fu et al., 2023; Nony et al., 2022; Busoso et al., 2022) employ a single global basis constructed by applying POD on a combination of multiple flow cases. The global basis maintains the benefits of POD, namely orthogonality and physical interpretability (VerHulst and Meneveau, 2014; Andersen et al., 2017; De Cillis et al., 2021). Using a global basis for constructing generic ROMs enables consistent physical analysis across different flow conditions using the same basis. It therefore holds the potential for constructing more robust POD models (Bergmann et al., 2009) including diverse forms of interpolation across parameter space to predict unseen flow cases.

Previously, Andersen and Murcia Leon (2022) qualitatively compared the resulting global POD modes to local POD modes derived from individual flow cases, but the efficiency of these bases was not compared. This article quantifies the efficiency of the global POD modes in reconstructing wind turbine wake aerodynamics compared to a local basis for a single flow case. Furthermore, a global POD basis is expected to converge as more flow cases are added (Haasdonk, 2013; Hesthaven et al., 2016), but the selection of which flow cases to include to ensure fast convergence is uncertain. Here, the convergence of the global basis is investigated in accordance with previous studies (Haasdonk et al., 2011; Hesthaven et al., 2016; Quarteroni et al., 2016). The analysis uses a database of large eddy simulations (LESs) of wind turbine wake dynamics, which are particularly challenging as they are highly turbulent and include a vast range of turbulent scales in the atmosphere. Therefore, this work contributes by explicitly showcasing the advantages and characteristics of global bases in ROMs applied in a practical yet complex scenario.

2 Methodology

2.1 Flow solver and turbine modeling

The LES database is the same as used for creating the predictive and stochastic reduced-order model of wind turbine

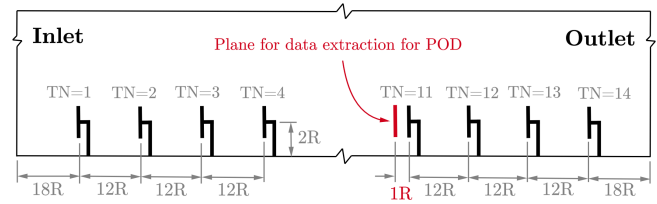


Figure 1. Simulation layout.

wakes (Andersen and Murcia Leon 2022), where the simulations were generated using the incompressible finite volume flow solver EllipSys3D (Michelsen, 1992; Michelsen, 1994; Sørensen, 1995). A third-order QUICK scheme is used for the convective terms, and a second-order implicit method is used for time stepping. The pressure correction equation is solved with an improved version of the SIMPLEC algorithm (Shen et al., 2003), and pressure decoupling is avoided using the Rhie–Chow interpolation technique. LES applies a spatial filter on the Navier–Stokes equations, where the smaller scales are modeled through a sub-grid-scale (SGS) model to achieve turbulence closure. The Deardorff SGS model is used (Deardorff, 1980).

The turbines are modeled using the actuator disc (AD) method, which imposes body forces in the flow equations (Mikkelsen, 2004). Initially, the velocities are passed from EllipSys3D to Flex5 (Øye, 1996), which computes the forces and deflections through a full aero-servo-elastic computation and transfers these back to EllipSys3D (Sørensen et al., 2015; Hodgson et al., 2021). The turbine modeling does not include the effects of the nacelle or tower, but this only has a minor influence on the wake-generating thrust (Zahle and Sørensen, 2008).

2.2 Simulation setup

The wind farm is simulated with 14 turbines aligned as shown in Fig. 1. The computational domain is $192R \times 20R \times 20R$ in the streamwise, lateral, and vertical directions, respectively. The grid is structured and has $3392 \times 192 \times 128 \approx 83 \times 10^6$ grid cells. The grid is equidistant from the inlet to the turbines and in the vicinity of the turbines, where it expands $\pm 4R$ on each side of the turbine center, as well as $4R$ vertically. This equidistant region has a resolution of approximately 20 cells per blade radius, which is highly resolved for AD simulations (Hodgson et al., 2023). The grid is stretched towards the lateral, top, and outlet boundaries.

The turbines are separated by $12R$ in the streamwise direction, and $20R$ in the lateral direction. Cyclic boundary conditions are imposed on the lateral boundaries to mimic an infinitely wide wind farm. The modeled turbine is the NM80 turbine, which has a radius of $R = 40.04$ m, hub height of $z_0 = 80$ m, and rescaled rated wind speed of $U_{\text{rated}} = 14 \text{ m s}^{-1}$, with a corresponding rated power of $P_{\text{rated}} = 2.75 \text{ MW}$ (Aagaard Madsen et al., 2010).

The neutral atmospheric boundary layer (ABL) inflow to the farm is modeled in a prior precursor simulation (Andersen and Murcia Leon, 2022). The initial precursor simulation has a roughness of $z_0 = 0.05$ m and a friction velocity of $u_* = 0.4545$ m s^{-1} , which resulted in an average shear exponent of $\alpha = 0.14$. The rough-wall boundary layer can be rescaled to model different wind speeds (Castro 2007).

The flow database consists of vertical planes of inflow to each rotor, which captures the wake aerodynamics generated by the upstream wind turbine(s). Therefore, the three velocity components are extracted in vertical planes of $2R \times 2R$ located one radius upstream of each turbine to reduce the turbine-specific influence of induction (Troldborg and Meyer Fosting, 2017); see Fig. 1. This corresponds to a grid of 39×42 points in the y - z plane. The time step is 0.1 s for simulations with $U = 8, 12, 15$ m s^{-1} and 0.05 s for $U = 20$ m s^{-1} . The data are extracted every 0.1 s during 2^{17} time steps, which is approximately 3.64 h of simulated flow.

2.3 Parameter space and flow characteristics

The database is designed to cover the majority of the operational range for this particular wind farm and therefore the parameter space governing the turbulent wake flow. The most important parameter for wind turbine wakes is the thrust coefficient C_T (van der Laan et al., 2020):

$$C_T = \frac{T}{\frac{1}{2}\rho AU^2}, \quad (1)$$

where T is the turbine’s thrust, ρ is the air’s density, A is the rotor’s area, and U is a representative velocity, typically the mean freestream axial velocity. This coefficient is a relative measure of the force exerted by the turbine with respect to the momentum of the incoming wind. For low wind speeds, the turbine extracts as much energy as possible, and the thrust coefficient is typically around 0.8, which is considered high. Significantly higher values can result in flow reversal as the turbine enters propeller mode (Sørensen et al., 1998). For high wind speeds, the turbine typically pitches its blades to reduce power extraction and thrust force.

Four simulations were performed for different average incoming wind speeds, which cover a significant range of operating thrust coefficients. A second parameter inherently present in a wind farm is the turbine number (TN). As the flow enters the wind farm, the incoming wind for the first turbine is undisturbed, but the second turbine operates in the wake of the first turbine. Further inside the wind farm, multiple wakes can be present concurrently. Wakes have a significant impact on the performance of wind farms, as the wind speed is lower and the turbulent intensity is higher, causing a reduction in power production and increased fatigue loads on turbines operating in the wake (Vermeer et al., 2003; Porté-Agel et al., 2020).

The parameter space covered by the database is visualized in Fig. 2. It consists of two parameters: turbine num-

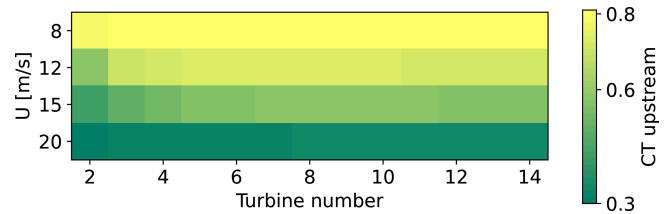


Figure 2. Parameter space from the large eddy simulations. C_T is shown for the upstream turbine for each mean wind speed in the simulation inlet and turbine number.

ber (2–14) of turbines operating in wake conditions and four wind speeds at hub height for the front turbine (8, 12, 15, and 20 m s^{-1}). Combined, these parameters are associated with a time-averaged C_T of the upstream wind turbine, which generates the wake. C_T is higher for low wind speeds until the turbine starts pitching. C_T is approximately constant through the wind farm at 0.8 and 0.3 for the cases of $U = 8$ m s^{-1} and $U = 20$ m s^{-1} , respectively. However, for $U = 12$ – 15 m s^{-1} , there is a gradual transition in C_T from the first turbine to the turbines further into the farm. Eventually, the flow will reach a balance between extracted power and wake recovery (Calaf et al., 2010). This is often referred to as the fully developed or “infinite” wind farm and is typically reached after the first five to six wind turbines (Andersen et al., 2020). Reaching the fully developed wind farm flow essentially means that there is no discernible difference between the inflow to turbines operating deep inside the wind farm, and therefore a data point in the parameter space does not necessarily offer additional information. In total, Fig. 2 shows 52 different combinations of the four wind speeds (U) and 13 turbine numbers (TN), where each combination corresponds to a dataset of inflow to a given turbine, $V(y, z, t)$.

2.4 Proper orthogonal decomposition

Proper orthogonal decomposition (POD) is a classic technique for dynamic flow analysis, which decomposes a turbulent flow into modes of spatial variability. These modes are orthogonal and, given the norm used to perform the decomposition, optimal in terms of capturing the variance of the fluctuating flow (Lumley, 1967; Berkooz et al., 1993).

The velocity field (V) is described as the sum of the mean flow (\bar{V}) and the fluctuating flow (V'), as in Eq. (2).

$$V(y, z, t) = \bar{V}(y, z) + V'(y, z, t) \quad (2)$$

POD is then applied to the three fluctuating velocity components of V' (u' , v' , and w'), where each time step is represented as a column vector, and N_t time steps are aggregated into a matrix $M = [V'_1, \dots, V'_{N_t}]$. The auto-covariance of M is computed as $R = M^T M$, and the eigenvalue problem $R\mathbf{G} = \mathbf{G}\mathbf{\Lambda}$ is solved, where $\mathbf{\Lambda}$ is a matrix of real and positive eigenvalues and \mathbf{G} is a matrix of orthonormal eigenvectors $\mathbf{G} = [g_1, \dots, g_{N_t-1}]$. The dimensionality has been re-

duced by 1 due to the extraction of the mean flow, and the orthonormality of the global modes is given using the standard inner product, $\langle a; b \rangle = a_i b_i$, across all flow components: $\langle g_i; g_j \rangle = \delta_{ij}$. Finally, the modes are organized according to the eigenvalue decay, i.e., in descending order according to variance, representing the turbulent kinetic energy contribution of each mode. Collectively, all modes form a new set of basis functions spanning the dataset.

The original flow can be reconstructed by projecting the flow into each mode with a standard inner product, which results in its contribution as a function of time (ϕ_i). Subsequently, as shown in Eq. (3), the modes multiplied by their contribution over time can be summed to reconstruct the flow.

$$V'(y, z, t) \approx \sum_{i=0}^K g_i(y, z) \phi_i(t) \quad (3)$$

An approximated reconstruction of the flow can be obtained by only including a limited number of modes ($K \leq N_{t-1}$).

2.5 Global POD basis

POD is traditionally applied on an individual flow case, i.e., on a “local” dataset in the parameter space. Therefore, applying POD on a single dataset is referred to as a *local POD basis* in the present work. The local basis contains the modes, which optimally represent the variance of that particular dataset. Conversely, a *global POD basis* is formed by including multiple datasets in the decomposition (Andersen and Murcia Leon, 2022).

The global basis can be computed by including q different datasets and adding N_T snapshots from each flow dataset to the matrix \mathbf{M} before applying POD:

$$\mathbf{M} = \left[V'_{1,1}, \dots, V'_{1,N_T}, \dots, V'_{q,1}, \dots, V'_{q,N_T} \right]. \quad (4)$$

Consequently, the global POD basis is sub-optimal at capturing the variance for a particular dataset, but it is expected to provide a better representation across the entire parameter space.

2.6 Convergence of global POD basis

The expected sub-optimality of a global POD basis raises several questions on how effective a global basis is compared to a local basis – for example, how many datasets should be used and which datasets should be included to create a global basis with high-quality performance across the parameter space compared to a local basis. Here, the parameter space contains 52 datasets. This means that for any number of datasets k composing a global base, there are $\binom{52}{k}$ possible global basis, so there are $\sum_{k=1}^{52} \binom{52}{k} = 4.5 \times 10^{15}$

possible combinations to generate a global basis, which effectively excludes the option of evaluating all of them. Consequently, the global POD bases are constructed in an iterative manner. First, a POD basis is based on a single dataset (one flow case in the parameter space), and its performance is evaluated across all flow cases of the parameter space. Secondly, a new flow case is added, and POD is applied to find the corresponding new basis, which is “global” because it was formed with more than one dataset. The new global basis is again evaluated across all flow cases before a new dataset can be added. In each iteration, the next dataset added to the decomposition corresponds to the flow case with the maximum error across the parameter space, thereby maximizing the reduction of the overall error. The iterative procedure means that only 52 different combinations exist, as each dataset can be chosen as the initial starting point.

3 Results

3.1 Flow cases

The wake flows change considerably across the parameter space. Figure 3 shows the normalized average streamwise velocity and the turbulence intensity for the four corners of parameter space (Fig. 2).

Figure 3a shows a significantly larger deficit and a more circular wake when C_T is high ($U = 8 \text{ m s}^{-1}$) and a less significant wake and more dominant shear profile from the atmospheric boundary layer when C_T is low ($U = 20 \text{ m s}^{-1}$). Furthermore, the spatial gradients are less pronounced late in the wind farm ($TN = 14$), which is a consequence of the increased mixing due to the presence of multiple wakes. Figure 3b shows the streamwise turbulence intensity ($\sigma(u')/U$), which ranges from 12% up to 23%, with the largest values in flows with a high thrust coefficient. The highest turbulence intensity is located in the upper half of the domain, where more momentum is exchanged between the wake and the surrounding atmospheric flow.

Figure 4 shows the streamwise velocity spectra taken at the rotor center for the four corners of the parameter space. This exemplifies how turbulent dynamics depend on both the thrust coefficient and turbine number. The total turbulent kinetic energy is larger for the high wind speed, as expected. The spectra tend to shift at the low frequencies, particularly for high C_T , as the largest turbulent length scales are broken down as they move through the wind farm (Andersen et al., 2017).

3.2 Global modes

POD is applied to compute the local and global POD bases. Figure 5 shows the first eight local modes calculated with one dataset from the parameter space, 1P. The figure also shows eight global POD modes derived using nine datasets, 9P. The local and global modes are clearly similar and are therefore

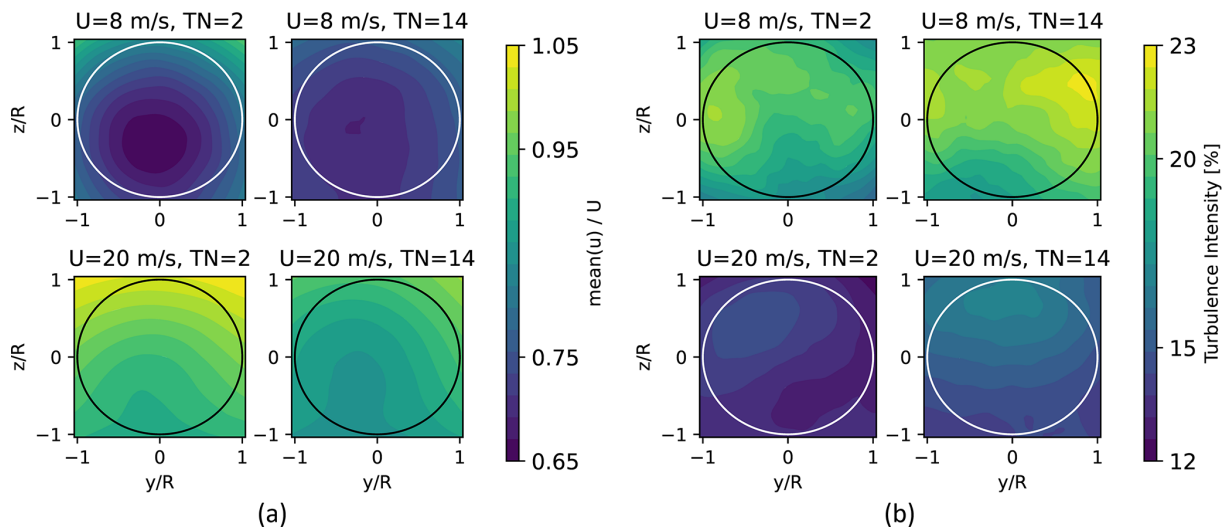


Figure 3. Flow characteristics at the four corners of the parameter space. The circle on each plot represents the rotor. **(a)** Mean wind speed in the streamwise direction. **(b)** Turbulence intensity.

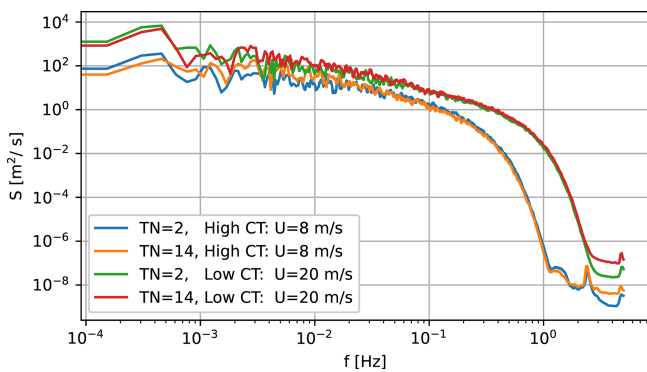


Figure 4. Fourier spectra of u' at hub height for the four corners of the parameter space.

capable of capturing the same coherent structures. However, the ordering of individual modes might change as they cover an increasingly large parameter space. This is an important point of the global basis. For instance, global mode 9P g_7 is not shown as it qualitatively corresponds to local mode 1P g_9 , while global modes 9P g_7 and 9P g_8 are more important over the parameter space. As shown by Andersen and Murcia Leon (2023), this means that the contribution of variance captured by each mode might change over the parameter space.

Although the local and global modes are qualitatively comparable, the global basis must be both efficient and representative of the entire parameter space. Figure 6 shows instantaneous flow fields for all velocity fluctuations U' , V' , and W' for LES and reconstructions using the first 20 modes of P1 and P9 for flow case $U = 20 \text{ ms}^{-1}$ and the fifth wind turbine, corresponding to the bases visualized in Fig. 5. The filtering effect of POD is clearly seen in the reconstructions

for both P1 and P9 for all velocity components, as the details of the LES are not reconstructed with only 20 modes. However, the overall structures of the reconstructed flow fields are comparable, particularly for the streamwise fluctuations U' . The region of positive fluctuations (red) in W' is slightly larger in P1, while P9 has a larger region without fluctuations (white) of W' . The figure also shows the difference in the instantaneous fluctuations from LES and the two reconstructions. The error fields of the two reconstructions are basically indistinguishable, with only minor differences. Appendix A shows the reconstructions and the corresponding errors using 8, 50, and 100 modes. The similarity in both reconstructed velocities and errors clearly shows that the two different bases are equally efficient at reconstructing the flow for all practical purposes.

3.3 Global modes convergence

In order to quantify the efficiency, a given basis is evaluated against the full LES flow using a velocity error E_{vel} defined in Eqs. (5) and (6). The metric takes, for every velocity component, the average in space (y, z) of the ratio between the root mean square error of the velocity field and its standard deviation over time. The error is normalized by the standard deviation because it is a direct measure of the variance in the original flow. Subsequently, E_{vel} corresponds to the norm of the errors from the three velocity components. This results in a single value for each point in the parameter space that represents the total error of the reconstruction with respect to the original flow.

The velocity error is shown in Fig. 7a, where the top-left figure corresponds to the local basis using one dataset of $U = 8 \text{ ms}^{-1}$ and $\text{TN} = 14$, indicated by the white number. This basis is evaluated across the entire parameter space us-

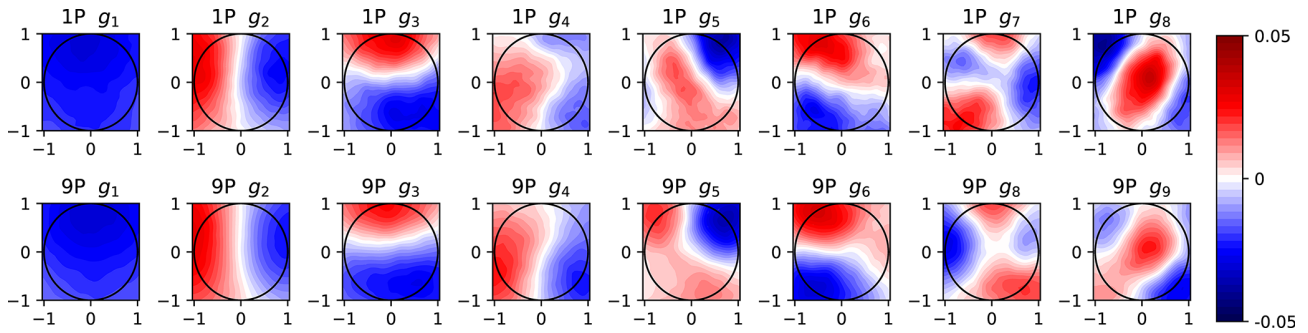


Figure 5. Streamwise component of the first modes using one and nine points from parameter space, 1P and 9P, respectively. The circle on each mode represents the turbine rotor.

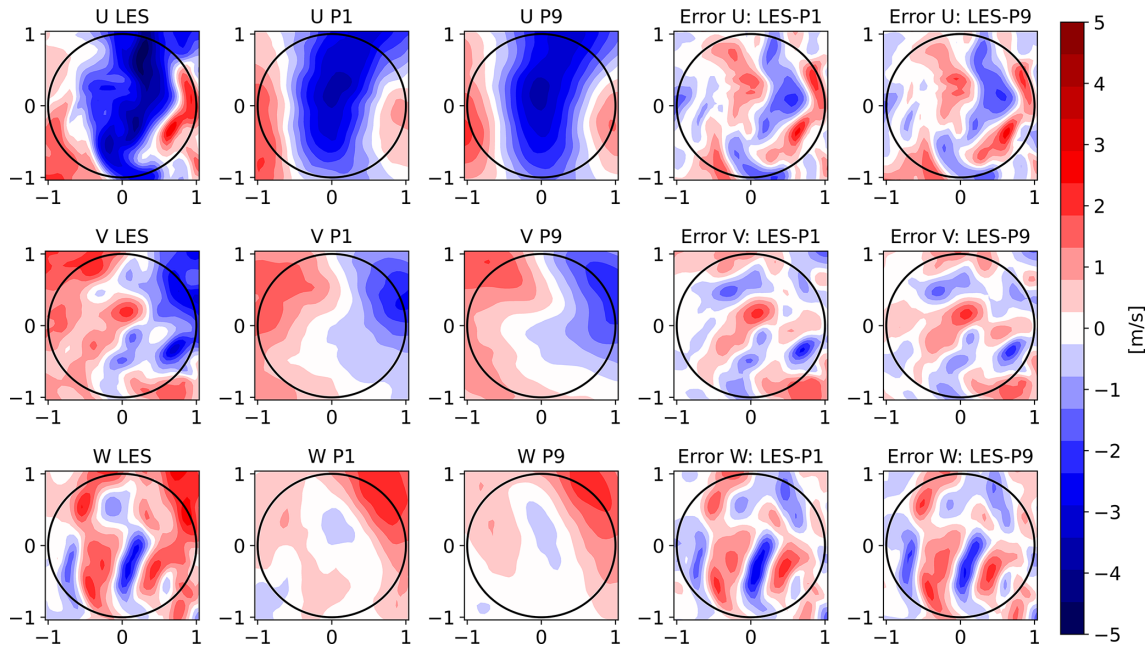


Figure 6. Flow fields of LES, reconstruction using P1 and P9, and error computed as the difference between LES and the reconstructed flows using 20 modes for the fifth turbine and $U = 20 \text{ m s}^{-1}$. The top row shows streamwise velocity fluctuations U' , the center row shows lateral velocity fluctuations V' , and the bottom row shows vertical velocity fluctuations W' .

ing 100 modes; i.e., the basis derived from the one dataset is applied on all flows. It reveals that the velocity error is largest at the first turbines for $U = 8 \text{ m s}^{-1}$. However, the error of the reconstructed flow compared to the LES is low for the high wind speed. Hence, the global basis provides efficient reconstruction for significantly different flow cases.

$$E_{u'} = \text{mean}_{y,z} \times \left[\frac{\sqrt{\text{mean}_t [u'_{\text{LES}}(y, z, t) - u'_{\text{POD}}(y, z, t)]^2}}{\text{std}_t [u'_{\text{LES}}(y, z, t)]} \right], \quad (5)$$

$$E_{\text{vel}} = \sqrt{E_{u'}^2 + E_{v'}^2 + E_{w'}^2}. \quad (6)$$

The velocity error (E_{vel}) corresponds to the total error with respect to LES, but this has two components: a truncation error due to the number of modes included and a basis error E_{basis} due to the use of a global basis, which is a non-optimal basis locally. The basis error arises because the global basis is sub-optimal compared to the local basis, which in principle is capable of reconstructing a larger portion of the flow with the same number of modes. Therefore, in order to isolate and quantify the basis error, the velocity error from the local POD bases ($E_{\text{vel-local POD}}$) is subtracted from E_{vel} , as shown in Eq. (7).

$$E_{\text{basis}} = E_{\text{vel}} - E_{\text{vel-local POD}} \quad (7)$$

The basis error is shown in Fig. 7b. In contrast to the velocity error E_{vel} , the largest basis errors correspond to the low C_T . Hence, the dataset for $U = 20 \text{ m s}^{-1}$ and $TN = 2$ with the largest basis error is added to improve the global

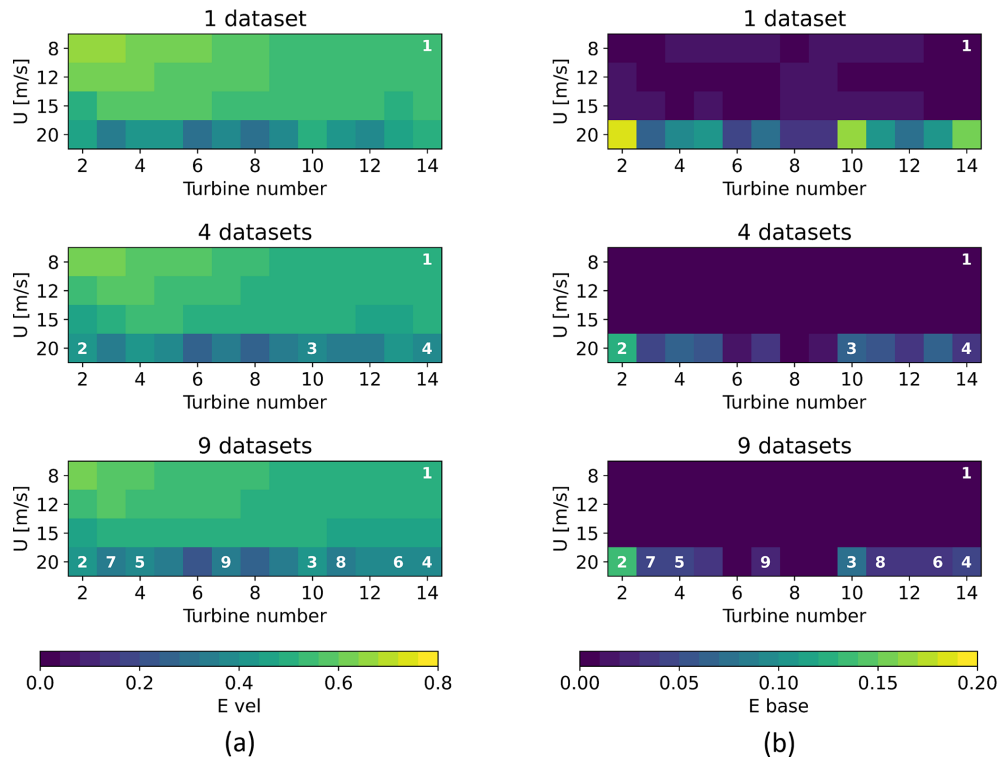


Figure 7. (a) Velocity error, E_{vel} , and (b) basis error, E_{basis} . Calculated using 100 modes across the parameter space for a basis including 1, 4, and 9 datasets.

Table 1. Initial datasets from parameter space.

Coordinates	Name				
	A	B	C	D	E
$U [ms^{-1}]$	8	20	8	20	15
TN	2	2	14	14	5

basis. The same error estimates are computed with the updated global basis, and the procedure is iterated to reduce the overall error of the global basis.

Figure 7 shows the evolution of errors using four and nine datasets. The white numbers indicate the order of adding the different datasets to the global basis. The average errors are clearly reduced when more datasets are included. Additionally, the largest basis errors remain at low C_T , and the difference of including one or four datasets is significantly larger than using four or nine datasets, which suggests the convergence of the global basis.

Figure 7 uses $U = 8 \text{ ms}^{-1}$ and $TN = 14$ as the initial dataset for the iterative procedure. Table 1 shows five different starting points. The first four initial datasets correspond to the four corners of parameter space, and the fifth is a point in the middle of the domain.

Figure 8 shows the evolution of the average velocity error (E_{vel}) across parameter space as a function of the number of datasets in the global basis for the five different initial conditions. As seen, all five initial conditions (A–E) yield the same trend of decreasing the mean velocity error as more datasets are included. On average the mean velocity error decreases 6% from one to nine datasets. Effectively, the choice of the initial dataset increasingly loses importance as more datasets are included. For instance, with one dataset, the relative difference between the best- and worst-performing global basis is 3.9%, but with nine datasets it is reduced to 0.4%. Furthermore, after including three datasets, the iterations starting at points B and D (those which started at $U = 20 \text{ ms}^{-1}$) contain the same datasets, which means that from that point they yield the same results.

The examined bases A–E include 512 snapshots per dataset, and the flow reconstruction was truncated at 100 modes. The horizontal lines in Fig. 8 indicate the average error when each flow in the parameter space is reconstructed with 100 modes of the corresponding local basis, computed using 512, 1024, and 2048 snapshots, respectively. The performance of these bases depends on the number of snapshots before achieving convergence, and the number of independent snapshots is limited, at around 2048, by the span of a single dataset. Independence is here based on snapshots being separated according to the integral length scales. On the

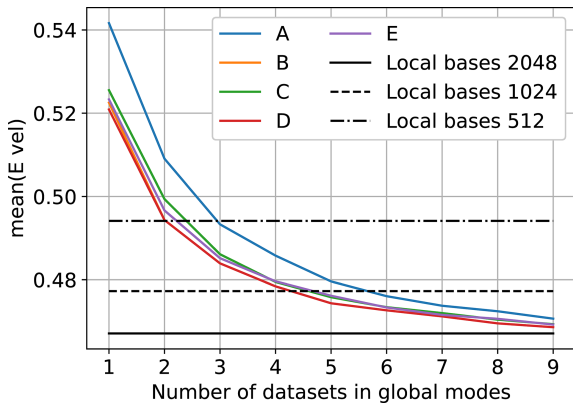


Figure 8. Mean error E_{vel} across the parameter space using 100 modes vs. the number of datasets included in the global basis.

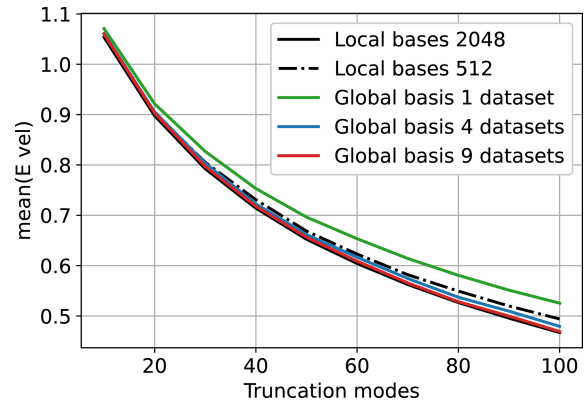


Figure 9. Mean error E_{vel} across the parameter space vs. number of truncation modes. The global bases shown correspond to the starting point C from Table 1.

other hand, a global basis can include more data because it is extracted from different datasets, i.e., different flows, which makes the snapshots independent.

Consequently, global bases can be directly compared to local bases when computed with the same amount of data. Table 2 compares the values of the horizontal lines in Fig. 8 (local bases error) with the average result from curves A–E at the corresponding number of snapshots. As more datasets are included, the performance of the global bases gets closer to the theoretical minimum error of the local bases, where four datasets correspond to a relative difference in the error of 2.8% truncated at 100 modes.

For the dependence of the number of truncation modes, Fig. 9 shows the velocity error for two local and three global bases truncating at different numbers of modes. Overall, the error decreases as more modes are included. Here, it is also possible to compare the truncation error to the basis error. The basis error is approximately 1 order of magnitude smaller than the truncation error. For instance, using 100 modes, the error of the global basis using 1 dataset is 0.523, and the error of the best bases, i.e., local bases 2048, is 0.469, which is a relative difference of approximately 10%.

It is noteworthy, especially for a global basis with a low number of datasets, that the basis error increases as more modes are included for the number of modes plotted. This is attributed to the fact that each additional mode from the optimal basis adds more information to the flow than a mode from the sub-optimal base. However, any of these bases are capable of completely reconstructing the flow if all modes are included. Therefore, it is expected that as more modes are included, the optimal bases start to saturate, while the sub-optimal bases eventually will catch up and the basis error gap will reduce.

3.4 Case study with stochasticity

The physical and statistical implications of employing a global basis are investigated using the stochastic engine PS-

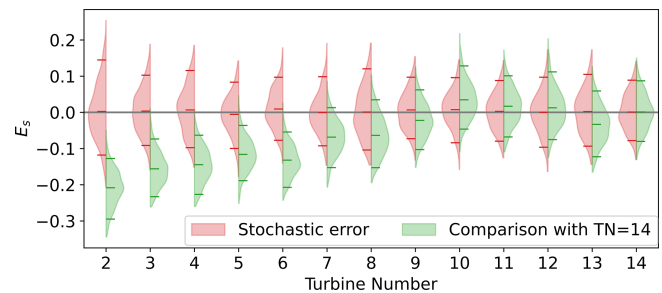


Figure 10. Distributions of spectral errors for the streamwise velocity at the rotor’s center related to the stochasticity and relative to turbine number 14 through the wind farm using 30 stochastic realizations and 100 global POD modes for the simulation case $U = 12 \text{ ms}^{-1}$.

ROM. The chosen global basis is generated based on four datasets shown in Fig. 7, which yield a basis error of 2.8%; see Table 2. The global basis is tested on the unseen flow case of $U = 12 \text{ ms}^{-1}$; i.e., the employed global basis does not contain information from this flow scenario.

The inherent stochastic variability is assessed by generating $N = 30$ stochastic realizations and cross-comparing all realizations against themselves for a single flow case. This yields a total of $\binom{N}{2} = 435$ stochastic flow realizations.

A general spectral error metric E_S of two spectrums is defined in Eq. (8):

$$E_{S-i,j} \equiv \frac{\int (\hat{S}_i - \hat{S}_j) df}{\int \hat{S}_j df}, \quad (8)$$

where S_i and S_j are the two spectrums to compare. \hat{S}_i is S_i filtered with a rolling mean using an averaging window varying logarithmically in size to smooth out higher frequencies.

Table 2. Mean velocity error comparison between local bases and global bases (average of curves A–E) with the same total number of snapshots using 100 modes.

Total number of snapshots	Local bases error	Global bases		Relative error difference [%]
		Number of datasets	Average error	
512	0.494	1	0.527	6.7
1024	0.477	2	0.499	4.6
2048	0.467	4	0.480	2.8

The spectral error is utilized in two ways, where the analysis is shown for the streamwise velocity at hub height.

First, the variability of the 30 stochastic realizations is estimated to provide stochastic error distributions, as shown in Fig. 10 for each turbine. The red distributions are all centered around zero and show the stochastic variability of the 30 realizations relative to themselves, i.e., how much can a single realization of a constructed flow scenario vary relative to numerous realizations of the same flow. The distributions tend to narrow further into the wind farm, which indicates how the deep farm flows become increasingly self-organized and governed by the wakes (Andersen et al., 2017).

Second, the development can also be examined by comparing the spectral error between different flows, i.e., comparing 30 stochastic flow realizations at each turbine against the inflow to a specific turbine. Here, the last turbine (TN = 14) is chosen to represent the fully developed wind farm. The spectral error given by Eq. (8) is also used for this comparison, which yields $N^2 = 900$ error samples since both flow cases have $N = 30$ stochastic realizations. The corresponding errors are shown as green distributions in Fig. 10. The distributions for the first turbines are significantly offset with a negative error but initially narrower than the stochastic distributions in red. Eventually, the green distributions gradually become centered around zero. Hence, the distributions of the stochastic spectral error and the spectral error relative to the 14th turbine can be compared directly to determine if there is a statistical difference between inflow to a given turbine relative to the last turbine. If the error distributions are reflections of each other, it implies that there is no statistical difference between the velocity spectra at the center of the domain between the turbine number in question and turbine number 14. This is particularly useful when trying to determine if the flow dynamics have reached the fully developed wind farm conditions, where the statistical distributions no longer change as the turbine number increases (Andersen et al., 2015). This is the case from approximately TN = 9 forwards.

The contribution of individual modes to the different flow cases can also be compared. Figure 11 shows similar spectral error distributions for global modes 2, 5, 12, and 20. Modes 2 and 5 show a gradual evolution reminiscing of Fig. 10, where the distributions gradually become increasingly similar. In contrast, higher modes, such as 12 and 20, present a more

scattered behavior, with lower errors and mean values varying between positive and negative for $TN > 2$, indicating more stochastic behavior. This suggests that the transition to a deep wind farm state is primarily dictated by changes in the first global modes, which are associated with the largest turbulent scales. This trend corroborates the findings of Andersen and Murcia Leon (2023), where it was clearly shown how different global modes are active in different locations within the wind farm to capture different flow scenarios, e.g., turbines operating in freestream conditions, turbines operating in single wake, or turbines operating in fully developed conditions.

3.5 Discussion

Employing a global POD basis allows the use of the same modes for an entire parameter space but introduces the basis error in the flow reconstructions (Eq. 7). The basis error emerges because the global basis is not as efficient at reconstructing a particular flow as the local POD basis. However, it was shown that this error is reduced as more datasets are included in the global basis, and it is approximately 1 order of magnitude smaller than the truncation error for 100 modes.

The convergence of the global POD basis as a function of the number of datasets has a parallel with the convergence of the local POD basis. A local POD basis converges when enough snapshots of the flow are included, so it contains information about all the dynamics that occur in the flow (Hekmati et al., 2011). Consequently, it is an optimal basis in terms of variance, and including more snapshots would not improve its performance. Similarly, the global POD basis will converge as more datasets are added to cover different flow dynamics across parameter space. Eventually, the performance of the basis will no longer improve by adding more datasets.

The inclusion of more datasets in the global basis implied adding more data in total, as the number of snapshots per dataset was kept constant. An alternative would be to keep the amount of snapshots constant and hence include fewer snapshots per dataset, which would reduce the time to compute the modes that scale quadratically with the number of snapshots. This is an unexplored scenario, but it is speculated that it would only be useful as long as there are enough snapshots per dataset to generate an acceptable local POD

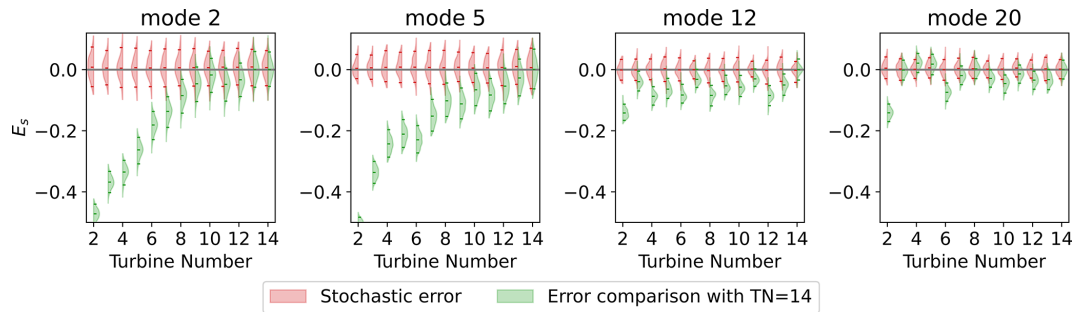


Figure 11. Distributions of spectral errors for four modes related to the stochasticity and relative to turbine number 14 through the wind farm using 30 stochastic realizations for the simulation case $U = 12 \text{ ms}^{-1}$.

basis with them, which would imply that there is enough information per dataset to capture its dynamics.

The systematic process of including additional datasets is focused on minimizing the basis error (Eq. 7) with respect to the local bases' performance. The iterative procedure particularly identifies that more datasets from flows corresponding to low C_T should be included. However, additional datasets could be identified using alternative metrics, e.g., the velocity error, which would prioritize adding datasets of low turbine numbers and high C_T . Applying such alternative metrics, or simply selecting datasets arbitrarily in the parameter space, also results in a reduction of the error as the number of datasets increases, and therefore the global basis will eventually converge on multiple error metrics. However, it might be impractical to perform a detailed and systematic convergence study of the global basis for all applications. Yet, the present analysis shows how global bases are relatively insensitive to which datasets are used. It is therefore generally recommended to select multiple datasets that represent various key flow phenomena. Selection of datasets a priori would typically require domain knowledge to identify key scenarios with different physics, e.g., single wake, multiple wakes, and different C_T values.

Furthermore, the case study highlights a number of benefits of employing a global basis. The global basis enables detailed and quantifiable physical interpretation of how the flow changes within the parameter space, as also seen in Andersen and Murcia Leon (2023), where the modal statistics of a global POD basis applied on a full wind farm clearly reveal three main flow regimes of atmospheric inflow, single wake, and multiple wakes. The expansion of the parameter space reveals new insights compared to Andersen and Murcia Leon (2022). For instance, it is clearly seen how the spectral error distributions converge further into the wind farm, indicating when fully developed wind farm flow dynamics are achieved and how this is linked to the first few modes (Fig. 11). The method also enables modelers to estimate both the impact and uncertainty of different flow realizations as well as different modes when generating synthetic turbulent flows. Additionally, the analysis reveals how wind turbine

wakes are relatively coherent flows, which can be covered by approximately 100 modes. Although, the consistently larger basis error for $U = 20 \text{ ms}^{-1}$ also highlights how more modes are required to reduce the errors for undisturbed atmospheric flows, where the influence of the turbines is negligible.

Finally, the global bases are used to model and analyze highly turbulent wind turbine wakes, and the present work expands the parameter space to cover two dimensions compared to the single parameter in Andersen and Murcia Leon (2022). In principle, there are no limits to the number of dimensions. However, it is speculated that the efficiency of global bases will significantly decrease if the parameter space covers multiple dimensions with very different flow cases. If so, more modes would be required for the flow generation. However, the efficiency and convergence of the linear global POD bases also promise that it is possible to utilize nonlinear dimensional reduction techniques, such as autoencoders, to increase efficiency further, *i.e.* reduce the number of modes required (Brunton and Kutz, 2019; Lee and Carlberg, 2019). Therefore, global bases are expected to be generally applicable for dimensional reduction within fluid dynamics.

4 Conclusions

Wind turbine wake aerodynamics are inherently complex and chaotic, thus making accurate modeling and analysis of their dynamics particularly challenging. One approach is to decompose the flow using POD, which gives an orthogonal basis of spatial modes. The spatial modes can provide physical insights into the largest coherent structures, and the modes can be used to develop reduced-order models. The modes are optimal in terms of capturing the variance, and the original flow can be reconstructed as the sum of a truncated set of modes, which fluctuate over time. However, different flows can result in different modes, which makes it difficult to construct general reduced-order models as well as compare different flows to provide insights into the physical differences. These caveats can be overcome by utilizing a global basis, where multiple flow cases are combined.

Global POD bases are shown to efficiently capture wind turbine wake aerodynamics for a parameter space covering all wake-affected turbines in a large wind farm during different operating conditions (thrust coefficients). The performance of the global basis has a basis error with respect to the optimal local POD basis. However, the error is 1 order of magnitude smaller than the truncation error, which can be remedied by including a few additional modes. Most importantly, the basis error is significantly reduced, and the efficiency convergence towards the local POD basis as more datasets are included to construct a global basis.

The efficiency is shown to be rather insensitive to the selection of flow cases to include in the construction of the global basis, especially when the basis error is compared to the truncation error of the flow reconstruction or the stochastic variability of flow realizations. However, it is recommended to include key features from the different flows in the parameter space.

Global bases also provide a consistent baseline for direct comparison of different flow cases and thereby enable physical interpretability of the flow behavior across the parameter space. For example, the evolution of the modes through the wind farm reveals that only the first few modes are responsible for the transition to a deep wind farm state, while higher modes corresponding to smaller turbulent structures mainly provide stochastic variations.

The convergence and benefits of global bases are illustrated here in the context of analyzing wind turbine wake flows with reduced-order models. However, the results are expected to generally apply to other turbulent flow scenarios; physical interpretation and model development are challenging.

Appendix A: Flow reconstruction and errors

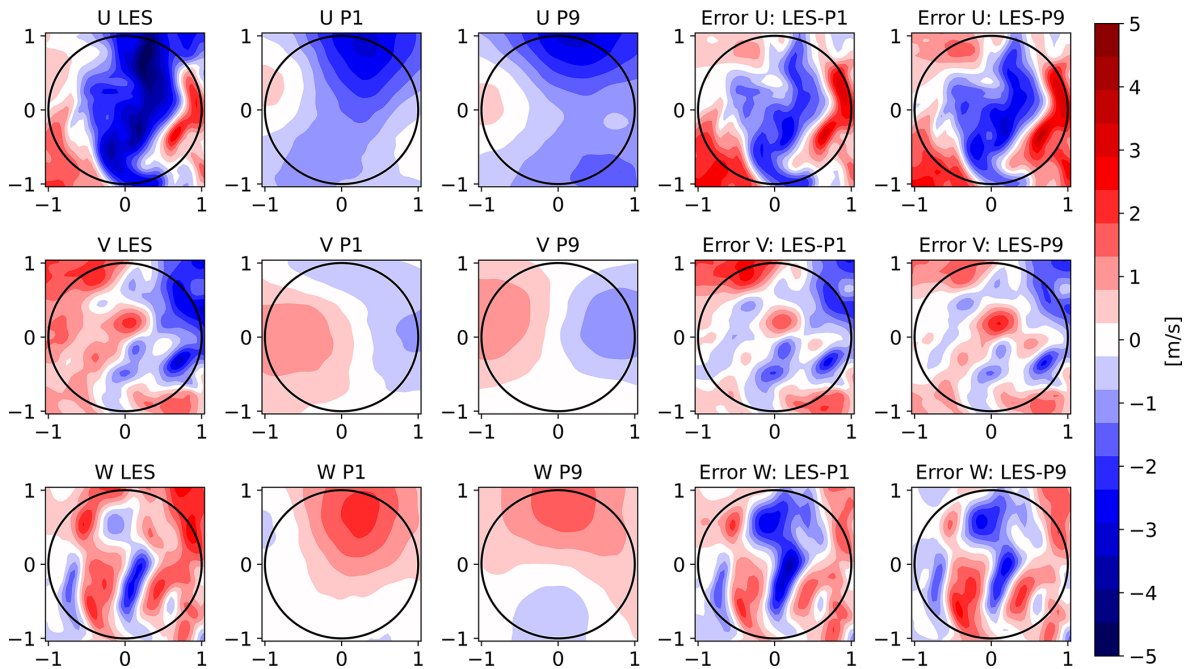


Figure A1. Figure 6 using eight modes.

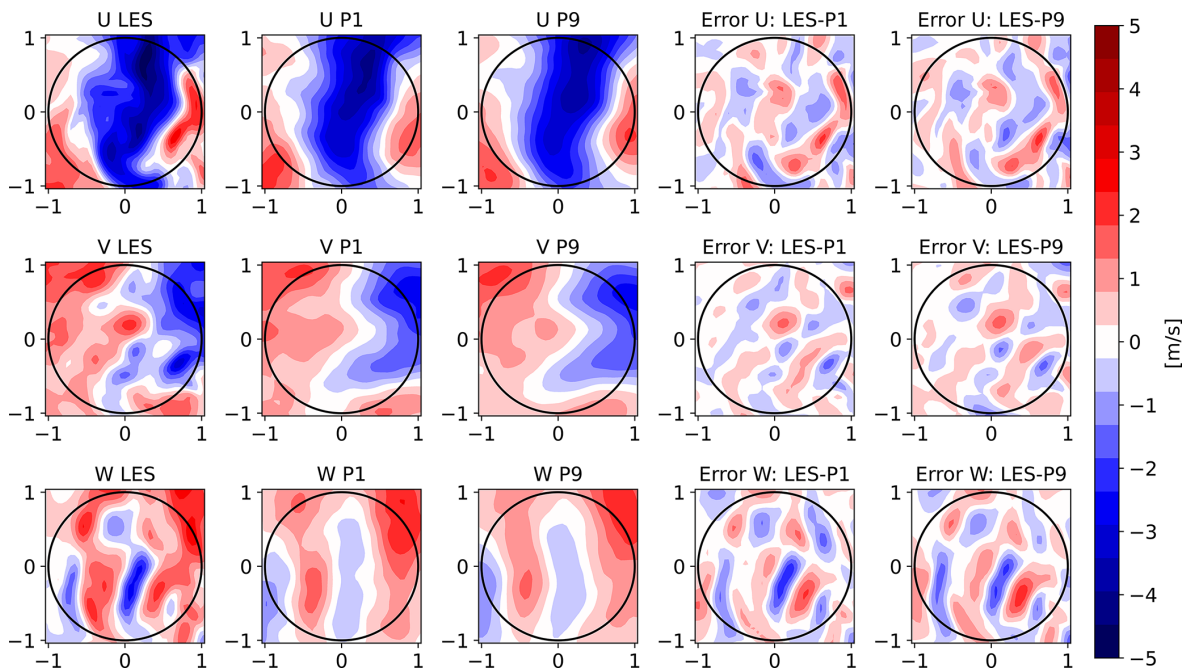


Figure A2. Figure 6 using 50 modes.

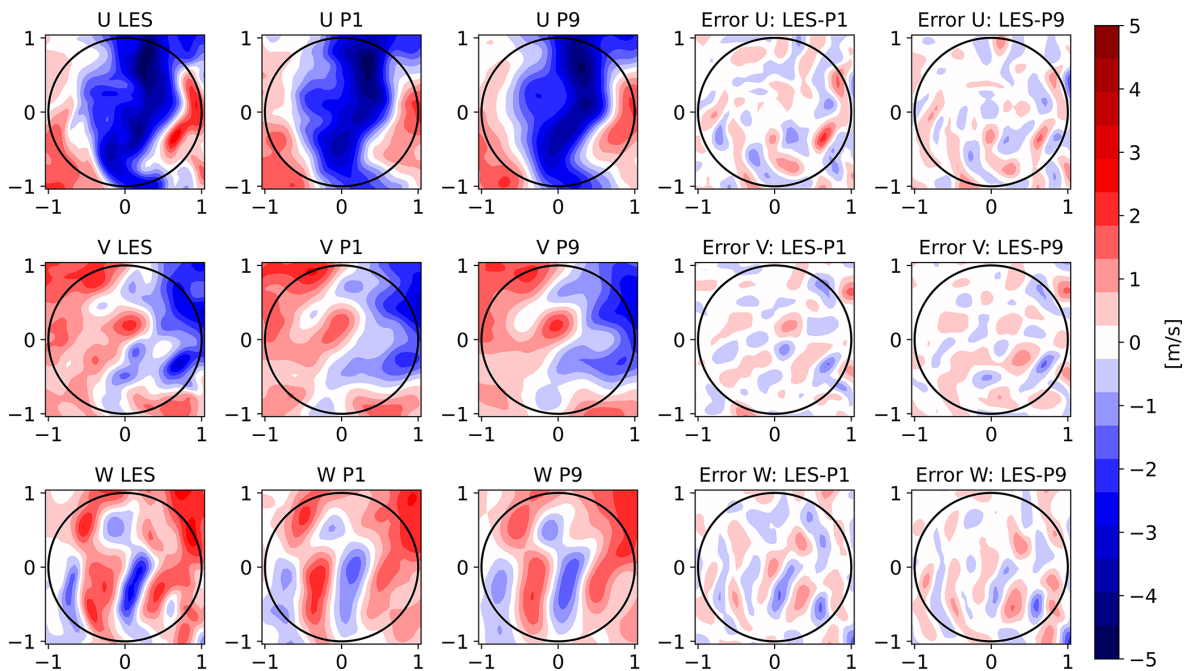


Figure A3. Figure 6 using 100 modes.

Code availability. The codes EllipSys3D and Flex5 are available with a license.

Data availability. Subsets of the datasets can be made available by contacting the authors.

Author contributions. The three authors conceived the idea of this article based on previous work developed by SJA and JPML. The LESs were done by SJA, and JFCM did the POD calculations and convergence of the global modes based on a code previously developed mainly by JPML. Finally, the writing and revision of this article were equally distributed among the three authors.

Competing interests. The contact author has declared that none of the authors has any competing interests.

Disclaimer. Publisher's note: Copernicus Publications remains neutral with regard to jurisdictional claims made in the text, published maps, institutional affiliations, or any other geographical representation in this paper. While Copernicus Publications makes every effort to include appropriate place names, the final responsibility lies with the authors.

Acknowledgements. Computational resources have been provided by the DTU cluster Sophia, DTU Computing Center, Technical University of Denmark (2022).

Financial support. This research has been supported by DTU Wind Energy through the Wind Farm Flow CCA 2022 and the MERIDIONAL project (<https://meridional.eu/>, last access: 7 March 2025) with grant agreement no. 101084216 under the European Union's Horizon 2020 research and innovation program.

Review statement. This paper was edited by Cristina Archer and reviewed by two anonymous referees.

References

- Aagaard Madsen, H., Bak, C., Schmidt Paulsen, U., Gaunaa, M., Fuglsang, P., Romblad, J., Olesen, N., Enevoldsen, P., Laursen, J., and Jensen, L.: The DAN-AERO MW Experiments: Final report, Danmarks Tekniske Universitet, Risø Nationallaboratoriet for Bæredygtig Energi, Forskningscenter Risø, Risoe-R No 1726(EN) in Denmark, 2010.
- Andersen, S. J. and Murcia Leon, J. P.: Predictive and stochastic reduced-order modeling of wind turbine wake dynamics, *Wind Energ. Sci.*, 7, 2117–2133, <https://doi.org/10.5194/wes-7-2117-2022>, 2022.

- Andersen, S. J. and Murcia Leon, J. P.: Stochastic wind farm flow generation using a reduced order model of LES, *J. Phys. Conf. Ser.* 2505, 012050, <https://doi.org/10.1088/1742-6596/2505/1/012050>, 2023.
- Andersen, S., Sørensen, J., and Mikkelsen, R.: Reduced order model of the inherent turbulence of wind turbine wakes inside an infinitely long row of turbines, *J. Phys. Conf. Ser.*, 555, 012005, <https://doi.org/10.1088/1742-6596/555/1/012005>, 2014.
- Andersen, S., Witha, B., Breton, S. P., Sørensen, J., Mikkelsen, R., and Ivanell, S.: Quantifying variability of large eddy simulations of very large wind farms, *J. Phys. Conf. Ser.*, 625, 012027, <https://doi.org/10.1088/1742-6596/625/1/012027>, 2015.
- Andersen, S. J., Sørensen, J. N., and Mikkelsen, R. F.: Turbulence and entrainment length scales in large wind farms, *Philos. T. Roy. Soc. A*, 375, 20160107, <https://doi.org/10.1098/rsta.2016.0107>, 2017.
- Andersen, S. J., Breton, S.-P., Witha, B., Ivanell, S., and Sørensen, J. N.: Global trends in the performance of large wind farms based on high-fidelity simulations, *Wind Energ. Sci.*, 5, 1689–1703, <https://doi.org/10.5194/wes-5-1689-2020>, 2020.
- Bastine, D., Bastine, D., Vollmer, L., Vollmer, L., Wächter, M., Peinke, J., and Peinke, J.: Stochastic wake modelling based on POD analysis, *Energies*, 11, 612, <https://doi.org/10.3390/en11030612>, 2018.
- Bergmann, M., Bruneau, C. H., and Iollo, A.: Enablers for robust POD models, *J. Comput. Phys.*, 228, 516–538, <https://doi.org/10.1016/j.jcp.2008.09.024>, 2009.
- Berkooz, G., Holmes, P., and Lumley, J. L.: The proper orthogonal decomposition in the analysis of turbulent flows, *Annu. Rev. Fluid Mech.*, 25, 539–575, <https://doi.org/10.1146/annurev.fl.25.010193.002543>, 1993.
- Brunton, S. L. and Kutz, J. N.: *Data-driven science and engineering: Machine learning, dynamical systems, and control*, Cambridge University Press, <https://doi.org/10.1017/9781108380690>, 2019.
- Buoso, S., Manzoni, A., Alkadhhi, H., and Kurtcuoglu, V.: Stabilized reduced-order models for unsteady incompressible flows in three dimensional parametrized domains, *Comput. Fluids*, 246, 105604, <https://doi.org/10.1016/j.compfluid.2022.105604>, 2022.
- Calaf, M., Meneveau, C., and Meyers, J.: Large eddy simulation study of fully developed wind-turbine array boundary layers, *Phys. Fluids*, 22, 015110, <https://doi.org/10.1063/1.3291077>, 2010.
- Castro, I. P.: Rough-wall boundary layers: mean flow universality, *J. Fluid Mech.*, 585, 469–485, <https://doi.org/10.1017/S0022112007006921>, 2007.
- Christensen, E. A., Brøns, M., and Sørensen, J. N.: Evaluation of proper orthogonal decomposition-based decomposition techniques applied to parameter-dependent non-turbulent flows, *SIAM J. Sci. Comput.*, 21, 1419–1434, <https://doi.org/10.1137/S1064827598333181>, 1999.
- Coloni, T., Rowley, C., Freund, J., and Murray, R.: On the choice of norm for modeling compressible flow dynamics at reduced-order using the pod, in: *Proceedings of the 41st IEEE Conference on Decision and Control*, 3, 3273–3278, <https://doi.org/10.1109/CDC.2002.1184376>, 2002.
- De Cillis, G., Cherubini, S., Semeraro, O., Leonardi, S., and De Palma, P.: Pod-based analysis of a wind turbine wake under the influence of tower and nacelle, *Wind Energy*, 24, 609–633, <https://doi.org/10.1002/we.2592>, 2021.
- Dear, J. W.: Stratocumulus-capped mixed layers derived from a three-dimensional model, *Bound.-Lay. Meteorol.*, 18, 495–527, <https://doi.org/10.1007/BF00119502>, 1980.
- Debnath, M., Santoni, C., Leonardi, S., Iungo, G. V.: Towards reduced order modelling for predicting the dynamics of coherent vorticity structures within wind turbine wakes, *Philos. T. Roy. Soc. A*, 375, 20160108, <https://doi.org/10.1098/rsta.2016.0108>, 2017.
- Fu, J., Xiao, D., Fu, R., Li, C., Zhu, C., Arcucci, R., and Navon, I. M.: Physics-data combined machine learning for parametric reduced order modelling of nonlinear dynamical systems in small-data regimes, *Comp. Method. Appl. M.*, 404, 115771, <https://doi.org/10.1016/j.cma.2022.115771>, 2023.
- George, W. K.: Insight into the dynamics of coherent structures from a proper orthogonal decomposition, *Proceedings of the International Centre for Heat and Mass Transfer, International Seminar on Wall Turbulence*, 16–20 May 1998, Dubrovnik, 469–487, http://www.turbulence-online.com/Publications/Journal_Papers/Papers/George88d.pdf (last access: 12 March 2025), 1988.
- Haasdonk, B.: Convergence rates of the pod-greedy method, *ESAIM-Math. Model. Num.*, 47, 859–873, <https://doi.org/10.1051/m2an/2012045>, 2013.
- Haasdonk, B., Dihlmann, M., and Ohlberger, M.: A training set and multiple bases generation approach for parameterized model reduction based on adaptive grids in parameter space, *Math. Comp. Model. Dyn.*, 17, 423–442, <https://doi.org/10.1080/13873954.2011.547674>, 2011.
- Hamilton, N., Viggiano, B., Calaf, M., Tutkun, M., and Cal, R. B.: A generalized framework for reduced-order modeling of a wind turbine wake, *Wind Energy*, 21, 373–390, <https://doi.org/10.1002/we.2167>, 2018.
- Hekmati, A., Ricot, D., and Druault, P.: About the convergence of POD and EPOD modes computed from CFD simulation, *Comput. Fluids*, 50, 60–71, <https://doi.org/10.1016/j.compfluid.2011.06.018>, 2011.
- Hesthaven, J. S., Rozza, G., and Stamm, B.: *Certified Reduced Basis Methods for Parametrized Partial Differential Equations*, Springer International Publishing, <https://doi.org/10.1007/978-3-319-22470-1>, 2016.
- Hinton, G. E. and Salakhutdinov, R. R.: Reducing the dimensionality of data with neural networks, *Science*, 313, 504–507, <https://doi.org/10.1126/science.1127647>, 2006.
- Hodgson, E. L., Andersen, S. J., Trolborg, N., Forsting, A. M., Mikkelsen, R. F., and Sørensen, J. N.: A quantitative comparison of aeroelastic computations using flex5 and actuator methods in LES, *J. Phys. Conf. Ser.*, 1934, 012014, <https://doi.org/10.1088/1742-6596/1934/1/012014>, 2021.
- Hodgson, E. L., Souaiby, M., Trolborg, N., Porté-Agel, F., and Andersen, S. J.: Cross-code verification of non-neutral ABL and single wind turbine wake modelling in LES, *J. Phys. Conf. Ser.*, 2505, 012009, <https://doi.org/10.1088/1742-6596/2505/1/012009>, 2023.
- Lee, K. and Carlberg, K. T.: Model reduction of dynamical systems on nonlinear manifolds using deep convolutional autoencoders, *J. Comput. Phys.*, 404, 108973, <https://doi.org/10.1016/j.jcp.2019.108973>, 2019.
- Lee, M. W. and Dowell, E. H.: Improving the predictable accuracy of fluid Galerkin reduced-order models us-

- ing two POD bases, *Nonlinear Dynam.*, 101, 1457–1471, <https://doi.org/10.1007/s11071-020-05833-x>, 2020.
- Lumley, J. L.: The structure of inhomogeneous turbulence, in: *Atmospheric turbulence and wave propagation*, edited by: Yaglom, A. M. and Tartarsky, V. I., 166–178, Moscow, 1967.
- Meyer, K. E., Pedersen, J. M., and Özcan, O.: A turbulent jet in crossflow analysed with proper orthogonal decomposition, *J. Fluid Mech.*, 583, 199–227, <https://doi.org/10.1017/S0022112007006143>, 2007.
- Michelsen, J. A.: *Basis3D – a Platform for Development of Multi-block PDE Solvers: beta – release*, volume AFM 92-05, ISSN 0590-8809, Technical University of Denmark, 1992.
- Michelsen, J. A.: *Block structured Multigrid solution of 2D and 3D elliptic PDE's*, Technical Report, AFM 94-06, ISSN 0590-8809, Technical University of Denmark, 1994.
- Mikkelsen, R. F.: *Actuator Disc Methods Applied to Wind Turbines*, PhD thesis, Technical University of Denmark, ISBN 87-7475-296-0, 2004.
- Neumann, J. and Wengle, H.: Coherent structures in controlled separated flow over sharp-edged and rounded steps, *J. Turbul.*, 5, N22, <https://doi.org/10.1088/1468-5248/5/1/022>, 2004.
- Noack, B., Morzyanski, M., and Tadmor, G.: *Reduced-Order Modelling for Flow Control*, Courses and lectures, Springer Wien New York, ISBN 978-3-7091-0757-7, 2011.
- Nony, B. X., Rochoux, M., Jaravel, T., and Lucor, D.: Reduced-order modelling for parameterized large-eddy simulations of atmospheric pollutant dispersion, arXiv:2208.01518, 2022.
- Olesen, P. J., Hodzic, A., Andersen, S. J., Sørensen, N. N., and Velte, C. M.: Dissipation-optimized proper orthogonal decomposition, *Phys. Fluids*, 35, 015131, <https://doi.org/10.1063/5.0131923>, 2023.
- Øye, S.: *Flex4 simulation of wind turbine dynamics*, 28th IEA Meeting of Experts Concerning State of the Art of Aeroelastic Codes for Wind Turbine Calculations, Lyngby-Denmark, April 1996, ISSN 0590-8809, 71–76, 1996.
- Porté-Agel, F., Bastankhah, M., and Shamsoddin, S.: Wind-turbine and wind-farm flows: A review, *Bound.-Lay. Meteorol.*, 174, 1–59, <https://doi.org/10.1007/s10546-019-00473-0>, 2020.
- Quarteroni, A., Manzoni, A., and Negri, F.: *RB Methods: Basic Principles, Basic Properties*, Springer, Cham, https://doi.org/10.1007/978-3-319-15431-2_3, 2016.
- Schmid, P. J.: Dynamic mode decomposition of numerical and experimental data, *J. Fluid Mech.*, 656, 5–28, <https://doi.org/10.1017/S0022112010001217>, 2010.
- Semaan, R., Kumar, P., Burnazzi, M., Tissot, G., Cordier, L., and Noack, B. R.: Reduced-order modelling of the flow around a high-lift configuration with unsteady coanda blowing, *J. Fluid Mech.*, 800, 72–110, <https://doi.org/10.1017/jfm.2016.380>, 2016.
- Shen, W. Z., Michelsen, J. A., Sørensen, N. N., and Sørensen, J. N.: An improved simplec method on collocated grids for steady and unsteady flow computation, *Numer. Heat. Tr. B-Fund.*, 43, 221–239, <https://doi.org/10.1080/713836202>, 2003.
- Sieber, M., Paschereit, C. O., and Oberleithner, K.: Spectral proper orthogonal decomposition, *J. Fluid Mech.*, 792, 798–828, <https://doi.org/10.1017/jfm.2016.103>, 2016.
- Sirovich, L.: Turbulence and the dynamics of coherent structures. I. Coherent structures, *Q. Appl. Math.*, 45, 561–70, <https://doi.org/10.1090/qam/910462>, 1987.
- Smith, T. R., Moehlis, J., and Holmes, P.: Low-dimensional models for turbulent plane couette flow in a minimal flow unit, *J. Fluid Mech.*, 538, 71–110, <https://doi.org/10.1017/S0022112005005288>, 2005.
- Sørensen, N.: *General purpose flow solver applied to flow over hills*, PhD thesis, Published 2003, Risø National Laboratory, ISBN 87-550-2079-8, 1995.
- Sørensen, J. N., Shen, W. Z., and Munduate, X.: Analysis of wake states by a full-field actuator disc model, *Wind Energy* 1, 73–88, [https://doi.org/10.1002/\(SICI\)1099-1824\(199812\)1:2<73::AID-WE12>3.0.CO;2-L](https://doi.org/10.1002/(SICI)1099-1824(199812)1:2<73::AID-WE12>3.0.CO;2-L), 1998.
- Sørensen, J. N., Mikkelsen, R., Henningson, D. S., Ivanell, S., Sar-mast, S., and Andersen, S. J.: Simulation of wind turbine wakes using the actuator line technique, *Philos. T. R. Soc. A*, 373, 20140071, <https://doi.org/10.1098/rsta.2014.0071>, 2015.
- Stankiewicz, W., Morzynski, M., Kotecki, K., and Noack, B. R.: On the need of mode interpolation for data-driven Galerkin models of a transient flow around a sphere, *Theor. Comp. Fluid Dyn.*, 31, 111–126, <https://doi.org/10.1007/s00162-016-0408-7>, 2017.
- Taira, K., Brunton, S. L., Dawson, S. T., Rowley, C. W., Colonius, T., McKeon, B. J., Schmidt, O. T., Gordeyev, S., Theofilis, V., and Ukeiley, L. S.: Modal analysis of fluid flows: An overview, *AIAA J.*, 55, 4013–4041, <https://doi.org/10.2514/1.J056060>, 2017.
- Technical University of Denmark.: *Sophia HPC cluster*, <https://doi.org/10.57940/FAFC-6M81>, 2022.
- Troldborg, N. and Meyer Forsting, A. R.: A simple model of the wind turbine induction zone derived from numerical simulations, *Wind Energy*, 20, 2011–2020. <https://doi.org/10.1002/we.2137>, 2017.
- van der Laan, M., Andersen, S., Kelly, M., and Baungaard, M.: Fluid scaling laws of idealized wind farm simulations, *J. Phys. Conf. Ser.*, 1618, 062018, <https://doi.org/10.1088/1742-6596/1618/6/062018>, 2020.
- VerHulst, C. and Meneveau, C.: Large eddy simulation study of the kinetic energy entrainment by energetic turbulent flow structures in large wind farms, *Phys. Fluids*, 26, 025113, <https://doi.org/10.1063/1.4865755>, 2014.
- Vermeer, N. J., Sørensen, J., and Crespo, A.: Wind turbine wake aerodynamics, *Prog. Aerosp. Sci.*, 39, 467–510, [https://doi.org/10.1016/S0376-0421\(03\)00078-2](https://doi.org/10.1016/S0376-0421(03)00078-2), 2003.
- Vinuesa, R. and Brunton, S. L.: Enhancing computational fluid dynamics with machine learning, *Nature Computational Science*, 2, 358–366, <https://doi.org/10.1038/s43588-022-00264-7>, 2022.
- Xiao, D., Fang, F., Pain, C., and Navon, I.: A parameterized nonintrusive reduced order model and error analysis for general time-dependent nonlinear partial differential equations and its applications, *Comput. Method. Appl. M.*, 317, 868–889, <https://doi.org/10.1016/j.cma.2016.12.033>, 2017.
- Zahle, F. and Sørensen, N.: *Overset Grid Flow Simulation on a Modern Wind Turbine*, 26th AIAA Applied Aerodynamics Conference, August 2008, Honolulu-Hawaii, <https://doi.org/10.2514/6.2008-6727>, 2008.